EUROFUSION WP19ER-CPR(20) 26698

V Chatzikos et al.

Evolution of microstructure in neutron irradiated cold rolled tungsten and its correlation with mechanical properties

Preprint of Paper to be submitted for publication in Special Issue of 31st Symposium on Fusion Technology (SOFT2020)

This work has been carried out within the framework of the EUROfusion Consortium and has received funding from the Euratom research and training programme 2014-2018 and 2019-2020 under grant agreement No 633053. The views and opinions expressed herein do not necessarily reflect those of the European Commission.

Evolution of microstructure in neutron irradiated cold rolled tungsten and its correlation with mechanical properties

V. Chatzikos[1,2], K. Mergia[1,*], E. Manios[1], S. Dellis[1], D. Papadakis[1,3], D. Terentyev[4], G. Bonny[4], A. Dubinko[4], I.E. Stamatelatos[1] and S. Messoloras[1]

[1]Institute of Nuclear and Radiological Sciences and Technology, Energy and Safety, NCSR Demokritos, Athens, 15310, Greece,
[2]Department of Physics, School of Sciences, University of Ioannina, Ioannina, 45110, Greece,
[3]Department of Physics, School of Sciences, University of Athens, Athens, 15772, Greece,
[4] SCK CEN, Nuclear Materials Science Institute, Boeretang 200, 2400 Mol, Belgium,

ABSTRACT

The understanding of the neutron irradiation effects in tungsten is of significant importance for its use as a plasma facing material in future fusion devices. In this study, cold rolled tungsten is neutron irradiated at the Belgian BR2 fission reactor at the temperatures 600, 800, 900 and 1200 °C to a dose of 0.18 dpa. The neutron induced changes in the microstructure are investigated as a function of irradiation temperature using transmission electron microscopy, positron annihilation spectroscopy and electrical resistivity measurements. The influence of the irradiation on the elastic properties and the hardness is examined using the impulse excitation techniques and depth-sensing indentation. Voids and dislocation loops are observed at all the irradiation temperatures. As irradiation temperature increases the number density of both voids and loops decreases whereas their size increases. The total dislocation density increases after irradiation at 600 °C whereas it decreases for higher temperature irradiations. Furthermore, the formation also of very small vacancy clusters in the temperature range of 800 - 900 °C is revealed by PAS measurements. The elastic properties are not influenced at this dose but a considerable hardening effect is found at all irradiation temperatures with the hardness reaching a maximum, of about 25%, at 800 °C and no significant changes occur at higher irradiation temperatures.

Keywords: fusion energy, tungsten, neutron irradiation, transmission electron microscopy, positron annihilation spectroscopy, mechanical properties, electrical resistivity

1 INTRODUCTION

The safe and prolonged operation of fusion reactors requires the use of plasma facing materials that can withstand high energy neutron irradiation, high heat fluxes, impact of highly energetic particles and cyclic stress loading [1]. Tungsten (W) is the prime choice for armor materials for the divertor and first wall in current and future fusion devices due to its attractive properties such as high melting point, high thermal conductivity, low tritium retention, good sputtering resistance, thermal stress and shock resistance and low swelling under irradiation [2,

* Corresponding author: K. Mergia, kmergia@ipta.demokritos.gr

3]. However, its brittle behavior at temperatures ranging from room temperature to several hundreds of degrees Celsius depending on the microstructure, limits its performance and therefore its potential for fusion applications. Several methods of microstructural modification have been proposed in order to improve the ductility and fracture toughness of tungsten. It has been shown that cold-rolling is a process which improves the ductility of W down to room temperature and at the same time results to a rather high strength material [4, 5].

In the literature there is a number of investigations regarding the microstructure and mechanical properties of tungsten and its alloys under fission neutron irradiation [6, 7, 8, 9, 10, 11, 12, 13, 14, 15, 16, 17, 18, 19, 20, 21]. Neutron irradiation results in extensive damage in the material that is revealed in the form of vacancy clusters or voids and dislocation loops. In addition, transmutation reactions produce Re, Os and Ta which diffuse and form precipitates. These three types of defect clusters, i.e. voids, dislocation loops and precipitates, can cause the increase of hardness and yield strength and decrease of tungsten's ductility. Dislocation loops prevail at temperatures below 500 °C [7, 13], whereas higher irradiation temperatures promote voids formation. Void lattice formation has been observed after irradiation at 550 °C to a fast neutron fluence of 10^{22} n/cm^2 [22]. It has been shown that the hardness and microstructure changes exhibit a clear dependence on the neutron energy spectrum [12].

In the current work we investigate the evolution of the microstructure of cold rolled tungsten irradiated at 0.18 dpa and in the temperature range from 600 to 1200 °C at the Belgian Material Test Reactor BR2. Open volume defects are determined by positron annihilation lifetime spectroscopy (PALS) and the irradiation induced changes in the microstructure by transmission electron microscopy (TEM). The impact of the irradiation induced microstructural changes on the elastic properties and hardness is assessed by impulse excitation technique and depth sensing instrumented indentation. In addition electrical resistivity measurements are employed to evaluate the microstructural evolution and the contribution of the radiation induced defects.

2 MATERIALS AND METHODS

2.1 Material and neutron irradiations

The tungsten material was produced by PLANSEE SE in sheet form using a powder metallurgical route consisting of sintering and rolling. The resulting material has a plate-like grain shape [23]. Disks with thickness of about 1 mm were sectioned using electrical discharge machining and were subsequently mechanically polished from both sides using diamond suspension up to 0.25 μm and colloidal silica at the final stage to obtain mirror quality surface and removing surface oxide and stresses/surface damage induced by the EDM cutting. The resulting thickness of the samples was about 0.5 mm.

Neutron irradiations were performed at the Belgian Material Test Reactor BR2. In order to maximize the fast-to-thermal neutron ratio and thus achieve transmutation rates of W into Re and Os closer to those expected under ITER and DEMO conditions, the irradiations were performed inside a fuel element and in the maximum fast neutron (> 0.1 MeV, 7×10^{14} n/cm^2/s) flux position.

The samples were encapsulated in 1.5 mm stainless steel tube filled with helium. The thickness of the steel tube was adjusted to maximize the shielding from the thermal neutrons. The gap between the samples and the tube was adjusted to achieve 600, 800, 900 and 1200 $^{\circ}$C following thermal and neutronic calculations. The irradiation dose was 0.18 displacement per atom (dpa), which was calculated by MCNPX 2.7.0 based on the total fast neutron fluence (8.9×10^{20} n/cm^2, >0.1 MeV) achieved after three irradiation cycles of a total duration of 70 days [24]. The dpa cross sections for W have been prepared from the JENDL4 file (MT444) for the threshold displacement energy of 55 eV, following the recommendation of IAEA [25].

2.2 Transmission Electron Microscopy

TEM was performed with JEOL 3010 TEM operating at 300 kV. The TEM samples were prepared by cutting the irradiated disks into pieces with a size of about 1.5 × 1.5 × 0.5 mm and then the coupons were mechanically polished using SiC paper with grit sizes of 220, 500, 1200, 2000 and 4000 to achieve 70-100 μm thickness. The coupons were rinsed in ethanol and then glued on 3 mm copper grids with an aperture of 1 mm. Finally, TEM specimens were polished electrochemically with a solution of 1.5 wt.% NaOH in water with applied voltage of 30 V. The local thickness of the specimen was determined from the CBED pattern and diffraction pattern. Several measurements in different areas were performed to make sure that the observed microstructure is indeed statistically representative. The average dislocation density was measured following the methodology used in [26]. The overall methodology for the registration of tungsten microstructure was adopted from our earlier works where the same tungsten grades were investigated after plastic deformation and high flux plasma exposure [27,28,29,30].

2.3 Positron annihilation spectroscopy

2.3.2 Positron Annihilation Lifetime spectroscopy (PALS)

PALS is is a powerful and sensitive method for the investigation of open volume defects with concentrations as low as 10^{-6} in materials [31, 32]. The positron when implanted in a material, it gets very fast (~10^{-12} s) thermalized and before it annihilates with an electron it may get trapped into defects. The positron lifetime in a defect is inversely proportional to the electron density seen by the positron. The reduced electron density at an open volume defect site, such as a vacancy, divacancy, dislocation or vacancy cluster, increases the positron lifetime, and the positron lifetime increases as the size of the open volume defect increases.

The principle of operation of the lifetime spectrometer is to measure the spectrum of time intervals between start signals, generated by detecting prompt gamma rays following the emission of positrons, and stop signals from one of the annihilation gamma photons. Positron annihilation lifetime measurements were carried out at room temperature using Ortec® PLS-system. The ^{22}Na radionuclide (from evaporated ^{22}NaCl metallic salt), with a half-life of 959.8 days, encapsulated in 3.6 mg/cm^2 thin polymide (Kapton®) windows, was used as the positron source with an activity of 100 μCi. The active area of the source is 5 mm. The positron source was sandwiched between two pieces of identical specimens. The 1.274 MeV gamma ray, indicating a positron emission event, and the two 0.511 MeV gamma rays of the positron annihilation event are detected using fast plastic scintillators coupled with photomultiplier (PM) tubes. The time resolution, i.e. the Full Width Half Maximum (FWHM) of the prompt spectrum,

was measured with ^{60}Co and energy windows set as for ^{22}Na and sample measurements and was found around 260 ps. The detectors were placed at a distance of about 5 mm from the sample. For each spectrum at least four million counts were collected.

The maximum penetration in tungsten of the positrons emitted by ^{22}Na (545 keV maximum energy) is around 50 μm, which is lower than the samples thickness, i.e. all positrons are annihilated inside the sample. The mean penetration depth of positrons having the mean energy of the ^{22}Na spectrum, i.e. 215 keV, is 11 μm, which is large enough to avoid any surface effects. On the other hand the two 0.511 MeV gammas emitted during the positron annihilation events have very small absorbance (~10%) by the tungsten material.

The data analysis was performed using LT10 software [33, 34]. The experimental spectra were fitted to the expression of the equation [33],

$$S(t) = B + R(t) \otimes \left(I_{src} + I_s \right) = B + R(t) \otimes \left(\sum_{k=1}^{L} I'_k e^{-\lambda_{src,k} t} + \sum_{i=0}^{N} I_i e^{-\lambda_i t} \right). \quad (1)$$

The components k refer to air, kapton and source part of the spectrum. The sample response I_s consists of N components with $i = 0$ referring to the defect free material and $i = 1, \ldots, N$ to the different open volume defects within the sample. Each component is characterized by the relevant intensity I_i and its lifetime $\tau_i = 1/\lambda_i$. $R(t)$ is the resolution function and B the background. In this expression it is assumed that in each defect the positron is annihilated independently of the other defects and the defect free matrix, i.e. there are no correlations.

Since positrons may annihilate both in the source materials (^{22}NaCl) and the thin foil encapsulating it, and these processes contribute additional lifetime components to the PALS spectrum it is essential to determine these components in order to obtain reliable values of the lifetimes and intensities of the W investigated samples. To this end, a number of reference well annealed materials (Al, Co, Ni, Cd and Pb) of high purity (better than 99.99%) were analyzed in order to determine the source parameters. Two source components were considered; one for the annihilations in the ^{22}Na source and Kapton® foil (because of their very similar lifetimes) and another one for the annihilations in the air between the source and the specimen.

In the analysis of all PALS spectra the resolution function was described by a sum of two Gaussians with FWHM of w_1 and w_2 and relative intensities i_{s1} and i_{s2} and a relative centroid shift t_s. The parameters of the resolution function were treated as fitted parameters for both the analysis of the reference samples and the W irradiated samples. In both cases the fitted values of all the parameters are in agreement.

The obtained lifetimes of the reference materials were found in very good agreement with the values reported in the literature (the details of this analysis are to be published in another paper). The lifetime value of the first source component, $\tau_{src,1}$, comprising the annihilations in the source itself and the surrounding Kapton® foil was found (371 ± 1) ps and it is in good agreement with values reported in the literature (in the range 368 - 386 ps for Kapton and NaCl source in [33, 35, 36], 385 ps for Kapton in [37]). The second source component, $\tau_{src,2}$, corresponding to the annihilations in the air between the source and the specimen, exhibits a lifetime value of (2.20 ± 0.03) ns and a small intensity of (2.0 ± 0.2) %.

2.3.3 Doppler broadening spectroscopy

Positron annihilation spectroscopy (PAS) was used to determine the coincidence Doppler broadening (CDB) spectrum in the irradiated samples. The CDB spectrum provides the momentum distribution of the electrons in the material. Thereby low momentum is associated to valence/free electrons, which are found near open volume and high momentum is associated to core electrons, which can be used to determine the chemical environment around a positron–electron annihilation site.

The CDB setup [38,39,15] consists of two movable high-purity Ge detectors (coaxial HPGe detector from Canberra type GC3018) with high-energy resolution (FWHM = 0.8 keV at 122 keV and FWHM = 1.8 keV at 1332 keV) and build-in preamplifier (model 2101P). A digital signal processor (DSP Canberra Model 2060) for each detector and personal computer with LabView acquisition board card were used to collect the spectra. Both the electronics (two detectors and coincidence) as well as the hardware (biological shielding and mobility of the detectors) were optimized to measure highly active specimen with moderate detector dead time (< 20%) and very low background.

The measurements were performed at room temperature using a ^{22}Na positron source. The positron source was sandwiched between two identical samples, such that the fraction of positron annihilations outside the samples is negligible.

The low and high-momentum regions in the CDB spectrum were quantified based on the S- and W-parameters, respectively. The S- and W-parameters were defined as the ratio of low momentum ($|c\ p_L| < 2.5 \times 10^{-3}\ m_0 c$) and high momentum ($15 \times 10^{-3}\ m_0 c < |c\ p_L| < 25 \times 10^{-3}\ m_0 c$) regions in the CDB spectrum to the total region, respectively. Here c denotes the lightspeed, m_0 the electron rest mass and p_L the longitudinal component of the positron-electron momentum along the direction of the γ -ray emission.

2.4 Electrical Resistivity

Electrical resistivity was measured employing the collinear 4-point probe (4PP) method using Keithley 2182A nanovoltmeter and Keithley 6221 AC and DC current source. The two outer pins of the 4PP probe are connected to a DC current source, while the two inner pins are connected to the nanovoltmeter. The ratio of the measured voltage to the supplied current is the 4PP resistance which has to be multiplied by a suitable geometric factor to give the resistivity of the sample [40, 41]. The geometric factor was calculated by combining Maxwell's equations for static fields with Ohm's law and the boundary conditions imposed by macroscopic geometric features (such as sample thickness and pins' spacing). By solving the resulting boundary value problem of electrostatic potential, it can be shown that the resistivity is equal to the product of the 4PP resistance with a function depending only on macroscopic geometric features. This function is the geometric factor and is useful in separating the measured 4PP resistance from resistivity which is a function of only the microstructure of the sample. The nanovoltmeter in combination with the current source were configured to operate as a single device in the so called "Delta Mode", where the current source is supplying a DC current with alternating polarity (reversing at a frequency of 24 Hz) in order to eliminate the effects of the thermal electromotive force (emf). The measurements were performed at 20 ^{o}C and the current used was in the range 10-100 mA.

2.5 Elastic Properties

The Young's modulus, E, the shear modulus, G, and the Poisson ratio, ν, of the non-irradiated and irradiated W(100) samples were obtained employing Impulse Excitation Technique (IET) [42] using the Buzz-o-Sonic system. For these tests, the disc shaped specimen was supported by a foam material and excited by a light mechanical impulse. The impulse tool used consisted of a steel ball (2 mm diameter) attached to the end of a thin elastic rod. A microphone located in the vicinity of the sample was used to transmit sound vibrations to the signal processing unit. The first and second natural resonant frequencies, $f_{1,2}$, are identified, which in turn can be used to calculate the values of $E_{1,2}$ corresponding to these frequencies using the following equation

$$E_{1,2} = \frac{3\pi r^4 f_{1,2}^2 \rho\left(1-\nu^2\right)}{K_{1,2}^2 t^2} \tag{2}$$

where ρ and t the density and the thickness of the sample. ν is determined according to ASTM E1876 [43] as a function of the ration of thickness versus radius, t/r, of the sample and f_1/f_2. $K_{1,2}$ are the first and second natural geometric factors listed in ASTM E1876 as a function of ν and t/r. G is determined using the equation

$$G = \frac{E}{2\left(1-\nu^2\right)} \tag{3}$$

2.6 Vickers hardness

Vickers depth sensing indentation experiments were performed employing NANOVEA's mechanical tester. The maximum load was set at 3 N, while the (un)loading rate was 20 N/min. A dwell time of 200 s was applied before starting of the unloading process. The loading rate was selected after a series of preliminary indentation tests to achieve stability in the hardness values. The holding time was chosen such as to attain equilibrium conditions, i.e. almost no change of the indentation depth. A set of nine indentation tests, spaced by 200 μm, were performed. An optical microscope was used to select the indented area free from visible defects. The hardness, H, of the samples was calculated using the projected area, A_p, of the residual imprint after the indentation tests determined from its optical microscopy images and the maximum applied force $F_{\max}$ through

$$H = \frac{F_{\max}}{A_p} = \frac{2F_{\max}}{d_{\text{mean}}^2}, \tag{4}$$

where d_{mean} is the mean diameter of the residual imprint.

3 RESULTS AND DISCUSSION

3.1 Microstructure characterization

3.1.1 TEM

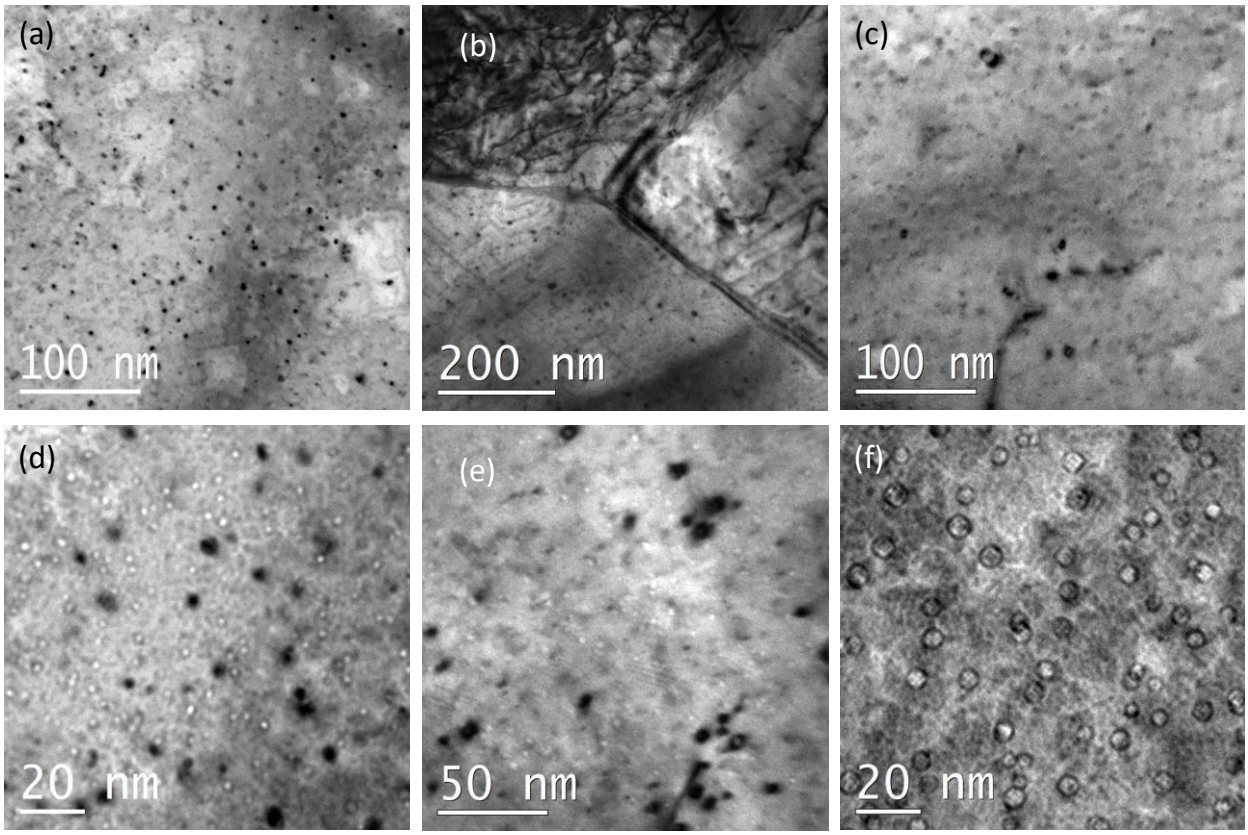

Fig.1. Bright field TEM images of the samples irradiated at (a,d) 600°C, (b,e) 800°C, (c,f) 1200°C. (a) T_{irr}=600°C overview of the loops (black dots) in dislocation-free region; (b) T_{irr}=800°C overview of the loops (black dots) nearby triple junction; (c) T_{irr}=1200°C overview of the loops (black dots); (f) T_{irr}=600°C voids in under focus contrast, loops are black objects; (e) T_{irr}=800°C voids in under focus contrast, loops are black objects; (f) T_{irr}=1200°C voids in under focus contrast.

Fig.1 shows the pattern of voids and loops in samples irradiated at 600, 800 and 1200°C. At 600°C, the mean size of the voids is 1.15 nm (density is 1.25×10^{23} m^{-3}) and the mean loop size is around 3 nm (density is 2×10^{22} m^{-3}). The voids were distributed homogeneously (see Fig.1d), while the loop's spatial distribution depended on the presence/absence of dislocation lines. In the dislocation-free region (see Fig.1a), the loops form random arrays, while near the dislocation lines the loops decorate dislocation lines. At 800°C, the mean size of the voids (see Fig.1e) has slightly increased up to 1.8 nm and density has slightly decreased down to 8.8×10^{22} m^{-3}. The formation of voids having a mean size of 3.8 nm and density 8×10^{21} m^{-3} has been observed in neutron irradiated pure tungsten after irradiation at 800 °C up to a dose of 0.98 dpa while after the irradiation at 500 °C no voids were observed [11]. The same authors

reported also the presence of dislocation loops with a mean size of 2.9 nm and density 3.3×10^{22} m^{-3} only at the lower irradiation temperature of 500 °C. The density of the loops has decreased by one order of magnitude, while the mean loop size decreased just slightly down to 2.66 nm. As in the case of 600 °C irradiation, the spatial distribution of the loops was found to depend on the particular area of observation being rich or depleted with dislocation lines, an example is shown in Fig.1b.

After the irradiation at 1200°C, both mean size of loops and voids has grown. At the same time, the density of the dislocation loops decreased nearly by two orders of magnitude (compared to that determined at 600 °C) going down to 7×10^{20} m^{-3}, see an example of the appearance of the loops in Fig.1c. The mean loop size has increased by a factor of three (3.81 nm vs. 1.15 nm at T_{irr}=600°C). The voids and (much less numerous) loops were seen to have homogeneous spatial distribution. The large voids have well pronounced faceted shapes as shown in Fig.1f.

The presence of the void lattice patterns was not observed in either of the investigated samples. Table I summarizes TEM findings for the voids, loops and dislocations at the various irradiation temperatures.

Table I. Radiation damage microstructural parameters obtained by TEM.

	Voids			**Loops**			**Dislocations**	**Total Dislocations**
T_{irr}	Diameter (nm)	Density (10^{23} m^{-3})	Volume fraction (%)	Diameter (nm)	Density (10^{22} m^{-3})	Volume fraction (%)	Density (10^{14} m^{-2})	Density (10^{14} m^{-2})
Unirradiated	-	-		-	-	-	1.0	1.0
600 °C	1.15	1.2	0.01	3	2.0	0.028	0.35	2.2
800 °C	1.83	0.88	0.028	2.66	0.317	0.0031	0.308	0.57
1200 °C	3.8	0.24	0.069	5.86	0.073	0.0077	0.175	0.31

3.1.2 Open volume defects using PALS

The normalized PALS spectra of the unirradiated and the irradiated W samples are presented in Fig. 2. It is observed that after irradiation the average positron lifetime increases compared to the unirradiated specimen.

As discussed in section 2.3.1 from PALS spectra the lifetime of defect free material and that of the different defects present in the samples are determined. Therefore, the association of the experimentally determined lifetimes with specific defects is essential. The lifetime that corresponds to the defect-free W materials is reported to be in the range 100-116 ps [44, 45, 46, 47, 48, 49, 50]. The lifetimes for mono-vacancy and dislocation defects are reported in the range of 160-200 ps and 130 – 180 ps, respectively [36, 46, 47, 51, 52]. The low lifetime value of 130 ps corresponds to screw dislocation as calculated by Staikov et al. [49]. Also the positron lifetime of a vacancy associated to either screw or edge dislocation was calculated in the range 188-192 ps [49]. Therefore in the range of lifetimes 160-200 ps the defects to be associated could be mono-vacancies and dislocations. The vacancy complex of 2-3 vacancies has been found to exhibit a lifetime of 230 ps [53, 54]. Lifetime values from 200 to 380 ps have been

reported as equivalent to average cluster sizes containing 1 to 9 vacancies [53, 55]. Voids having 13-37 vacancies have a lifetime of 410 - 440 ps [48], and a longest lifetime of 550 ps has been associated with large vacancy clusters containing more than 40 vacancies [53]. Therefore lifetimes above 200 ps are associated with vacancy agglomerates.

For the unirradiated sample two lifetimes are required to fit its PALS spectrum, a lifetime τ_0 ~100 ps which according to the discussion above corresponds to positron annihilations in the bulk defect free material and a second lifetime τ_1 having a value of (170 ± 1) ps which is attributed to positron annihilations at dislocations (Fig. 3). These dislocations have been created during the cold rolling fabrication process of the W material. The intensities I_0 and I_1 are almost equal demonstrating that the probabilities of a positron to be annihilated in the defect free material or in the dislocations are equal.

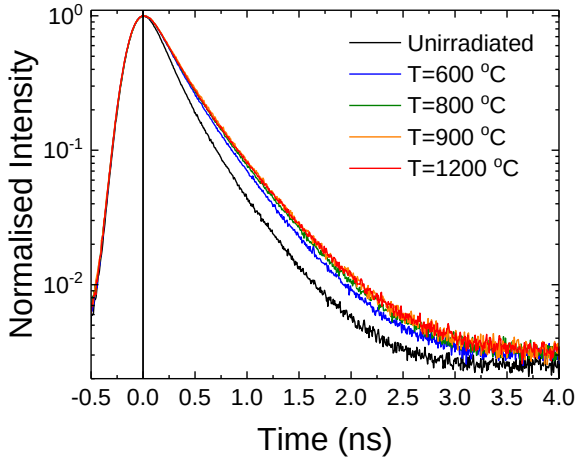

Fig. 2. PALS spectra for cold rolled W plate irradiated at 600, 800, 900 and 1200 °C and the unirradiated one.

Three positron lifetime components (τ_0, τ_1 and τ_2) were required to describe the PALS for all the irradiated samples (Fig. 3). The obtained lifetimes with their average τ_{av} together with their relative intensities versus irradiation temperature are presented in Fig. 3. In the fitting procedure the lifetime τ_0 was kept constant to that found in the unirradiated sample. The average lifetime shows a two-fold increase after irradiation at 600 °C, reflecting the creation of extensive open volume defects, whereas it increases almost linearly with the increase of the irradiation temperature from 600 to 900 °C. Further increase of the irradiation temperature does not change its value significantly.

The lifetime, τ_1, after irradiation at 600 °C is (163 ± 1) ps, close to that found for the unirradiated sample ((170 ± 1) ps). The defects associated with this lifetime in both the unirradiated and irradiated samples are dislocations [36, 46, 47, 51, 52]. As the irradiation temperature increases to 800 °C τ_1 increases to (205 ± 2) ps. This lifetime must be a weighted average of lifetimes corresponding to very small vacancy clusters of about 3 vacancies. Further

increase of the irradiation temperature to 900 °C causes the increase of τ_1 to (246 ± 6) ps which corresponds to a vacancy complex of 4-5 vacancies [48]. Irradiation at 1200 °C results in the decrease of τ_1 to (156 ± 5) ps, similar to the values of the uniradiated sample and that irradiated at 600 °C and reflecting positron annihilations at dislocations. Summarizing the results for τ_1, for irradiation at 600 and 1200 °C τ_1 is associated with dislocations only whereas at 800 and 900 °C τ_1 is attributed to both dislocations and small vacancy clusters.

After irradiation a second lifetime, τ_2, is observed with values ranging from 492 to 553 ps. This lifetime corresponds to positron annihilations at large vacancy clusters or voids having more than 40 vacancies [48, 53]. The obtained values for τ_2 show that for irradiation at 600 °C the voids have a diameter larger than about 1 nm, a value which is in agreement with TEM results. The lifetime τ_2 increases almost linearly with the irradiation temperature up to 900 °C and then it remains constant. The increase of τ_2 with irradiation temperature indicates larger number of vacancies in a cluster. For large vacancy clusters (>40 vacancies) theoretical calculations predict a small or no dependence of the positron lifetime on the void size [32, 48], due to the localization of positron at the cavity surface, with a saturation positron lifetime value of around 500 ps. Therefore, the increase of lifetime τ_2 with irradiation temperature reflects a increase in the size of the vacancy clusters which is observed also by TEM.

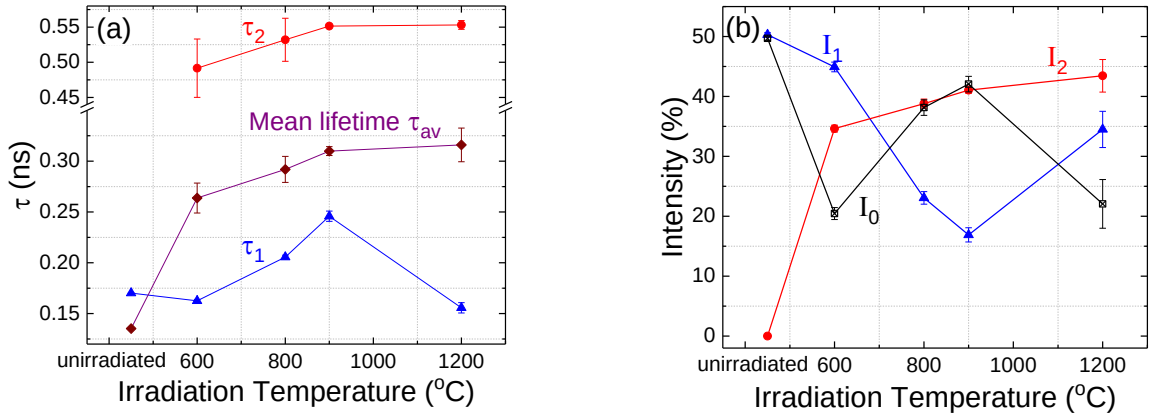

Fig. 3. Lifetime components (a) and their relative intensities (b) obtained from least square fit of equation (1) to PALS spectra for the unirradiated and irradiated cold rolled W plate at the various irradiation temperatures.

The intensities $I_i, (i = 0,1,2)$, reflect the probability of a positron being annihilated within the defect free matrix ($i = 0$) or a defect ($i = 1$ dislocation or monovacancy or small vacancy complex of up to 5 vacancies, $i = 2$ vacancy cluster of more than 40 vacancies). The relative probabilities ($I_i / I_0, i = 1,2$) reflect the extent of the defects in relation with the defect free regions. In the unirradiated sample $I_1 / I_0 \approx 1$, i.e. it is equal probable the positron to be

annihilated in a dislocation and in the defect free matrix. This indicates that ~50% of the sample can be considered as affected by the dislocations introduced by the cold rolling.

Irradiation at 600 °C increases this ratio to around 2.2, reflecting the dislocations arising from the irradiation. According to TEM results the total dislocation density increases from 1×10^{14} m^{-2} for the unirradiated sample to around 2.2×10^{14} m^{-2} for the sample irradiated at 600 °C (Table I, dislocation total density), and this increase is in excellent agreement with the obtained ratio I_1 / I_0. At 800 °C I_1 / I_0 is reduced by a factor of about 4 and the same reduction is observed in the dislocation density observed by TEM. As it has been discussed above there is an increase in the lifetime τ_1 and this increase has been associated with small vacancy clusters. As the decrease of the ratio I_1 / I_0 at 800 °C is equivalent to the decrease of the dislocation density the contribution of the vacancy clusters in I_1 could be assumed small. For the irradiation at 1200 °C the ratio I_1 / I_0 is 50 % higher than that of the unirradiated sample. On the contrary, the observed dislocation density by TEM is by a factor of three lower. As these two findings are inconsistent we might assume that other defects formed at 1200 °C and having annihilation times close to that of dislocations contribute. These could vacancy-impurity complexes according to [52].

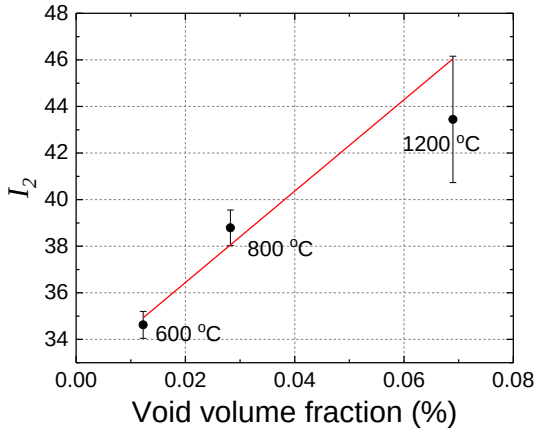

Fig. 4. Intensity I_2 corresponding to voids obtained from least square fit of eq. (1) to PALS data versus void volume fraction as determined by TEM measurements (Table I). The solid line is a linear least square fit to the data.

As discussed above the lifetime τ_2 and consequently the intensity I_2 have been attributed to large vacancy clusters or voids. As the irradiation temperature increases the intensity I_2 and the lifetime τ_2 increase almost linearly (Fig. 3). This increase of I_2 indicates the respective increase in the volume fraction of vacancy clusters under the assumption that the trapping strength for positrons remains constant and it is in very good agreement with the void's volume fraction as determined from TEM results (Table I) as it is shown by its almost linearly correlation with the volume fraction measured by TEM (Fig. 4).

3.1.3 Open volume defects using PAS-DB

In Fig. 5 the CDB spectra obtained at different irradiation temperatures are presented. The spectra focussed around the low momenta are shown in Fig. 5a, while the ones around the high momenta are presented in Fig. 5b. For the low momenta, the spectra for the irradiated samples increase significantly compared to the reference, while for the high momenta no obvious difference can be observed within the scatter. Although a measurable increase is measured for low momenta, little variation with irradiation temperature is observed. To check this increase in more depth, the *S*-parameter is computed. Computation of the *W*-parameter is omitted due to the large scatter (low statistics).

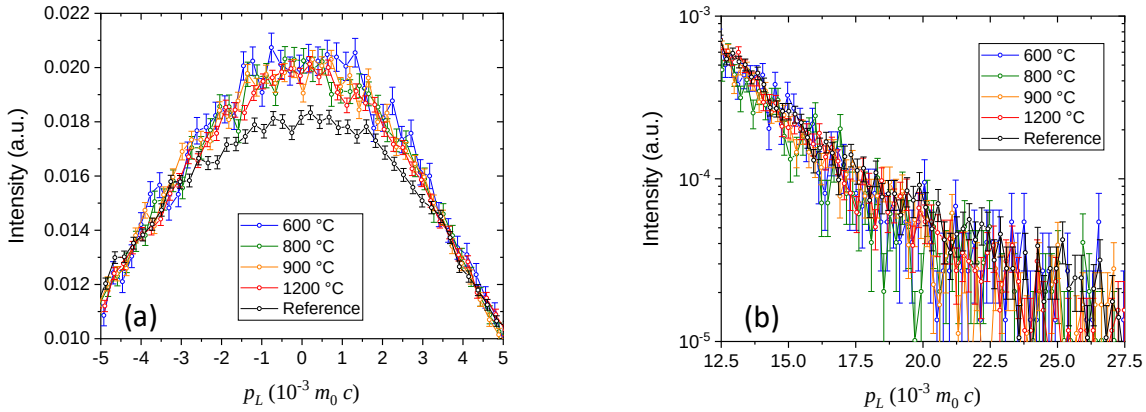

Fig. 5. CDB spectra for the different irradiation temperatures in the low momentum region (a), and high momentum region (b).

In Fig. 6 the *S*-parameter is presented as a function of irradiation temperature. Consistent with the CDB spectra, the *S*-parameter varies little with temperature: 11% at 600 °C and 8% at 1200 °C. Thus, even at the irradiation temperature of 1200 °C, a significant amount of open volume defects is still present in the material.

The slight decrease of *S*-parameter with irradiation temperature is consistent with a shift in vacancy cluster population towards larger clusters, as explained in [15]. This observation is consistent with the picture sketched following the PALS measurements.

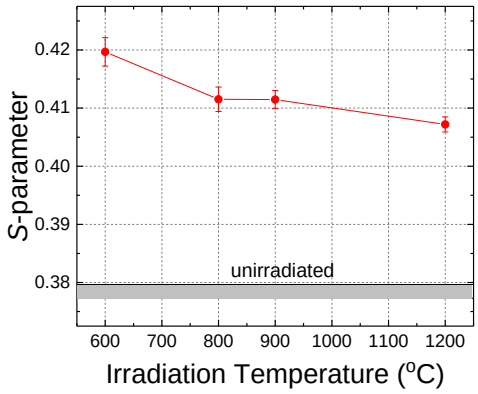

Fig. 6. *S*-parameter as a function of irradiation temperature.

3.1.4 Electrical Resistivity

The electrical resistivity of the unirradiated W material was found to be $(6.50 \pm 0.04)\ \mu\Omega\cdot\mathrm{cm}$. In the literature the reported resistivity value of high purity (99.99% or higher) W at 20 ^{o}C is $5.28\ \mu\Omega\cdot\mathrm{cm}$ for polycrystalline samples [56, 57]. The difference of $1.22\ \mu\Omega\cdot\mathrm{cm}$ between the resistivity of the W material used in the current study and the value reported in the literature is due to the dislocation induced by the cold-rolling process.

The resistivity of the irradiated samples was found higher than that of the unirradiated reflecting the additional electron scattering from the irradiation induced defects and transmutation products. By subtracting the resistivity of the unirradiated sample from that of the samples irradiated at the various temperatures, the Radiation Induced Resistivity (RIR) is derived. With this subtraction the electrical resistivity arising from the scattering of conduction electrons from phonons and also scattering arising from dislocations or other defects produced during the fabrication process of the material have been removed. Therefore, the result of this subtraction refers to the resistivity increase caused by the irradiation, i.e. from additional defects such as voids, dislocations and transmutation products.

The variation of RIR with the irradiation temperature is depicted in Fig. 7. The statistical error from the voltage - current measurements are of the order of 10^{-3} μΩ.cm or smaller. The mean value and the experimental errors in Fig. 7, which are of the order of 10^{-2} μΩ.cm, are calculated from the variation of the resistivity for different in-plane orientations of the collinear 4-point probe. The RIR for irradiation at 600 ^{o}C is the highest compared to all the other values measured for the irradiation temperatures 800 - 1200 ^{o}C. The increase of the irradiation temperature from 600 to 800 ^{o}C causes a decrease of RIR of about 30%. On the contrary, RIR exhibits a small increase of about 8.5% as the irradiation temperature increases from 800 to 1200 ^{o}C.

Further analysis of the electrical resistivity data requires their combination with available data from TEM measurements through the use of a simple quantitative model for the scattering of conduction electrons on the various types of defects and impurities. RIR can be considered as the sum of four main components (ignoring cross scattering of the electrons from the different defects)

$$RIR = RIR_{\mathrm{void}} + RIR_{\mathrm{loop}} + RIR_{\mathrm{line}} + RIR_{\mathrm{trans}} \tag{5}$$

where RIR_{void}, RIR_{loop}, RIR_{line} and RIR_{trans} are the contributions of voids (including mono- or cluster of vacancies), dislocation loops, dislocation lines and transmutation products, respectively.

The contribution of monovacancies to resistivity is proportional to their number density, if their concentration is small (e.g. of the order of 10^{-3} or smaller) and they are randomly distributed [58]. In the case of a vacancy cluster, a structure factor is needed for the description of the relative position of vacancies inside it [59]. Detailed calculations for the determination of the contribution of vacancy clusters to resistivity were performed by J. W. Martin et al. [60, 61, 62] and it was found that, for nearly spherical clusters, the corresponding resistivity can be described approximately by a power law dependence on the number n_{vac} of the vacancies in a cluster as

$$RIR_{\text{void}} \approx P_{1\text{V}} \cdot n_{vac}^{0.7} \cdot N_{\text{void}} = C \cdot (d_{void} / \alpha)^{2.1} \cdot N_{\text{void}} \quad (6)$$

where $P_{1\text{V}} \approx 10^{-34}\ \Omega \cdot \text{m}^4$ (K-D. Rasch et al. [63]) is the Vacancy Specific Resistivity (VSR), i.e. the resistivity corresponding to 1 monovacancy per m^3 and N_{void} (m^{-3}) is the number density of a vacancy clusters having n_{vac} vacancies. For a void of diameter d_{void} the first term of equation (6) results to the second one where α the W lattice constant and C a known constant ($1.033 \times 10^{-26}\ \mu\Omega \cdot \text{cm} \cdot \text{m}^3$). Using equation (6) and the density and diameter of the voids determined by TEM the RIR_{void} has been calculated and it is presented in Table II. The voids have a small contribution to RIR of 1.2% at 600 °C which increases to 3.3% at 1200 °C.

The transmutation products Re, Os and Ta have been evaluated by FISPACT-II nuclide inventory code and TENDL-2017 and EAF-2010 nuclear data bases (to be published). The calculated concentration for Os and Ta are about two orders of magnitude lower than that of Re and therefore only Re is taken into account for the calculation of RIR arising from the transmutation productions, thus

$$RIR_{trans} = P_{\text{Re}} N_{\text{Re}} \quad (7)$$

where $P_{\text{Re}} = 1.3\ \mu\Omega \cdot \text{cm}/(\text{Re at.}\%)$ the specific resistivity applicable to dilute W-Re alloys [64, 65]. However, the calculated Re concentration depends on the nuclear data base used (TENDL-17 or EAF-2010). The RIR arising from these two different sets of calculations and employment of equation (7) are presented in Fig. 7. As it can be seen the variation of RIR_{trans} with temperature is very small and thus it can be assumed as constant.

Regarding the contribution of radiation induced dislocations to RIR, it is considered that electrical resistivity due to dislocations is insensitive to the details of dislocation arrangement, since the main contribution to dislocation resistivity emerges from scattering of conduction electrons within a few Burgers lengths from dislocation lines [66] and, therefore, the effects of the dislocation cores dominate those of the long-range strain fields [67]. Due to this insensitivity to the details of dislocations arrangement, the contribution of dislocations to electrical resistivity is expressed as [68, 69, 70, 71]

$$RIR_{\text{line}} = P_{\text{DSR}} N_{\text{line}} \quad (8a)$$

where P_{DSR} the Dislocation Specific Resistivity, and N_{disl} the dislocation density. In the case of dislocation loops, equation (8a) takes the form

$$RIR_{\text{loop}}(d_{\text{loop}}) = P_{\text{DSR}} \cdot \pi d_{\text{loop}} \cdot N_{\text{loop}}(d_{\text{loop}}) \quad (8b)$$

where d_{loop} is the diameter of the dislocation loop and $N_{\text{loop}}(d_{\text{loop}})$ their number density. Therefore the RIR from both lines and loops, RIR_{disl} , can be written as

$$R_{\text{disl}} = RIR_{\text{line}} + RIR_{\text{loop}} = P_{\text{DSR}} \left[N_{\text{line}} + \pi d_{\text{loop}} \cdot N_{\text{loop}}(d_{\text{loop}}) \right] \quad (9)$$

There is a discrepancy between the values shown in the literature for P_{DSR} of W where three different values are reported for P_{DSR}: $7.5 \times 10^{-25}\ \Omega \cdot \text{m}^3$, $1.9 \times 10^{-24}\ \Omega \cdot \text{m}^3$ and

$6.7\times10^{-23}\ \Omega\cdot\mathrm{m}^3$ spanning two orders of magnitude [68, 69, 70, 71]. The measurement of P_{DSR} is based at measurements of deformed high purity materials at cryogenic temperatures (~4.2 K) where the contribution of electron-phonon scattering is practically zero, and the measured values are considered to be due to dislocations. However, impurities can never be completely removed and their presence may cause a correlation between electron-dislocation scattering and electron-impurity scattering in a metal, which results in the dependence of P_{DSR} on dislocation density [72, 73]. Dislocation densities smaller than a threshold value of about $10^{13}\ \mathrm{m}^{-2}$ at 4.2 K can result in overestimation of P_{DSR} of an order of magnitude [71]. A.S. Karolik *et al*. [71] concluded that the value of $6.7\times10^{-23}\ \Omega\cdot\mathrm{m}^3$ given for W in Ref. [69] is overestimated since it emerged from measurements in samples where the dislocation density was not high enough.

There are two limitations for comparing RIR experimental values versus the calculated ones. The first arises from the fact that the Dislocation Specific Resistivity, P_{DSR}, is not well established (in the literature it varies by two orders of magnitude, see discussion above) and the second is due to the fact that the contribution of the Re transmutation product depends on the specific nuclear data library used for the evaluation of its concentration (Fig. 7). As we require $RIR_{\mathrm{exp}} = RIR_{calc}$ and taking into account equations (5)-(9) we have

$$\begin{aligned} RIR_{\mathrm{exp}} &= RIR_{calc} = RIR_{\mathrm{trans,calc}} + RIR_{\mathrm{void,calc}} + P_{\mathrm{DSR}}\left(N_{\mathrm{disl}} + \pi\cdot d_{\mathrm{loop}}\cdot N_{\mathrm{loop}}\right) \\ RIR_{\mathrm{trans,calc}}\left(P_{\mathrm{DSR}}\right) &= \left(RIR_{\mathrm{exp}} - RIR_{\mathrm{void,calc}}\right) - P_{\mathrm{DSR}}\left(N_{\mathrm{disl}} + \pi\cdot d_{\mathrm{loop}}\cdot N_{\mathrm{loop}}\right) \end{aligned} \qquad (10)$$

As the densities of voids, dislocations and their sizes are known from TEM, $RIR_{\mathrm{trans,calc}}\left(P_{\mathrm{DSR}}\right)$ can be calculated if the correct value of P_{DSR} is known. As this is not the case, we may use the fact that $RIR_{\mathrm{trans,calc}}\left(P_{\mathrm{DSR}}\right)$ for the correct value of P_{DSR} should be a line almost parallel to x-axis as the concentration of Re transmutation produced defects is almost constant versus temperature. $RIR_{\mathrm{trans,calc}}$ has been calculated for two values of P_{DSR} ($3\times10^{-23}\ \Omega\cdot\mathrm{m}^3$ and $4\times10^{-23}\ \Omega\cdot\mathrm{m}^3$) shown in Fig. 7. Values outside these limits give values with large slopes so they have to be dismissed. Further we observe from Fig. 7 that $RIR_{\mathrm{trans,calc}}$ is in very good agreement with that evaluated using the Re concentration obtained employing EAF-2010 nuclear data base. Finally in Fig. 7 the calculated RIR using $P_{\mathrm{DSR}} = 3\times10^{-23}\ \Omega\cdot\mathrm{m}^3$ and RIR_{trans} evaluated using EAF-2010 nuclear data base is compared with the experimental data and a good agreement is obtained. The experimental and calculated values of resistivity as well the contribution of the different defects are presented in Table II in which a very good agreement between calculated and experimental values is observed.

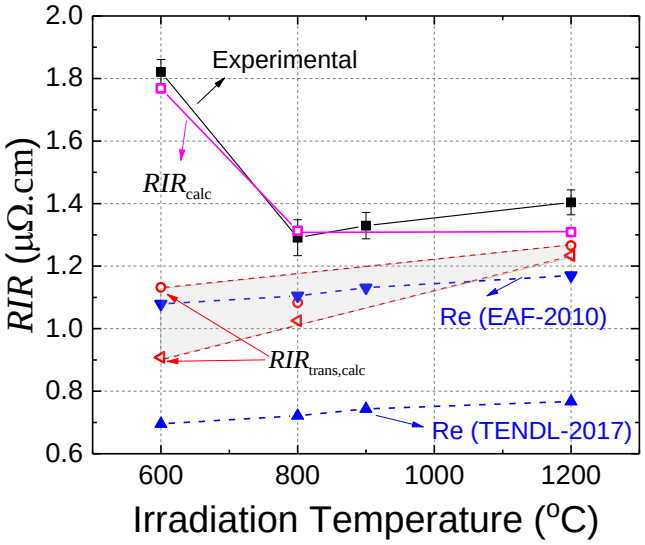

Fig. 7. Radiation induced resistivity, RIR, of the neutron irradiated cold rolled W plate samples to 0.18 dpa at various irradiation temperatures. (■): experimental data, (□): calculated using eq. (5) for $P_{DSR} = 3\times10^{-23}\ \Omega\cdot m^3$ and Re production according to EAF-2010, (▲, ▼): RIR_{trans}, calculated contribution from Re transmutation product using TENDL-2017 and EAF-2010 nuclear data base, (○, ◁): $RIR_{trans,calc}$, the difference between experimental data and that calculated values for the defects (voids, dislocations loops and lines) determined from the TEM data in Table I and equations (6), (9) and (10), using for P_{DSR} the values of $3\times10^{-23}\ \Omega\cdot m^3$ (○) and $4\times10^{-23}\ \Omega\cdot m^3$ (◁) (see text for details).

Table II. Experimental and calculated values for Radiation Induced Resistivity, RIR, for defects as determined from TEM measurements, and Re transmutation production using EAF-2010 nuclear data base.

	Experimental	**Calculated**	**Contribution to Calculated**		
T_{irr} (°C)	RIR (μΩ.cm)	RIR_{calc} (μΩ.cm)	RIR_{trans} (μΩ.cm)	RIR_{void} (μΩ.cm)	RIR_{disl} [1] (μΩ.cm)
600	1.82	1.77	1.08	0.019	0.67
800	1.29	1.31	1.11	0.036	0.17
1200	1.40	1.31	1.17	0.046	0.093

[1] For $P_{DSR} = 3\times10^{-23}\ \Omega\cdot m^3$

3.2 Mechanical Properties

3.2.1 Elastic Properties

The Young's modulus, E, shear modulus, G, and Poisson ratio, ν, of the non-irradiated and irradiated W plate were determined as described in Section 2.5 and are presented in Table III. The values for the unirradiated sample are in a good agreement with literature data which

are reported in the range 400 to 420 GPa, 158 to 163 GPa, and 0.278 to 0.282, for E, G and ν respectively [74, 75, 76]. The elastic properties of the irradiated sample remain the same, within error bars, with those before the irradiation. It can thus be concluded that neutron irradiation to a dose of 0.18 dpa for irradiation temperatures in the range 600 to 1200 ^{o}C does not affect the elastic properties of cold rolled sheet W.

Table III. Experimentally determined Young's modulus, E, shear modulus, G, Poisson's ratio, v, and hardness, $\langle H \rangle$, of unirradiated and irradiated cold rolled sheet W to 0.18 dpa.

T_{irr} (^{o}C)	E (GPa)	G (GPa)	ν	H (GPa)
Unirradiated	397 ± 6	156 ± 3	0.27 ± 0.03	5.15 ± 0.04
600	403 ± 6	158 ± 3	0.28 ± 0.03	6.04 ± 0.08
800	408 ± 6	162 ± 3	0.26 ± 0.03	6.44 ± 0.06
900	402 ± 6	159 ± 2	0.27 ± 0.03	6.29 ± 0.07
1200	400 ± 6	156 ± 3	0.28 ± 0.03	6.30 ± 0.09

3.2.2 Hardness

From the optically determined diameter of the Vickers' indenter imprint and equation 4, the hardness of the material was determined (Table IV). The hardness, H, of the unirradiated cold rolled W plate material was found (5.15 ± 0.04) GPa. Irradiation to 0.18 dpa at 600 ^{o}C increases the hardness by 17 % while irradiation at higher temperatures leads to a further increase of the hardness (Fig. 8). The highest hardness increase, ΔH, of about 25% is observed after irradiation at 800 ^{o}C, while further increase of the irradiation temperature does not affect hardness significantly.

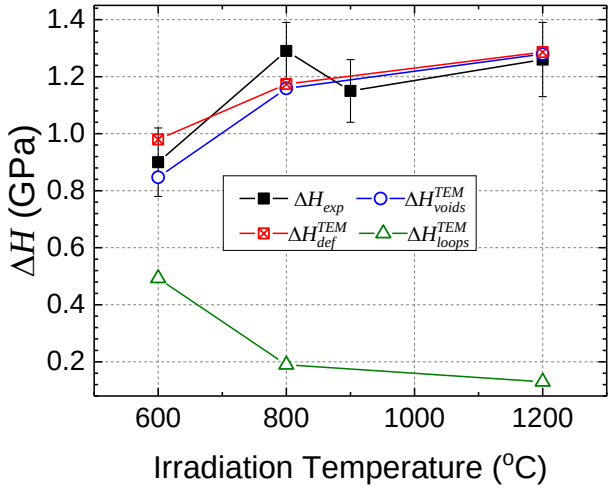

Fig. 8. Experimental (■) hardness increase versus irradiation temperature of cold rolled W sheet irradiated to 0.18 dpa. Calculated contributions employing eq. (13) and (14) and TEM data (Table I) from voids (○), loops (△) and the total of defects (☒) assuming root-sum-square law.

Subsequently, the dispersion hardening barrier (DHB) model is used to describe the radiation hardening in metals [11, 77]. According to the DHB model each type of defect induces an increase in the yield strength, $\Delta\sigma_{def}$, that can be expressed as

$$\Delta\sigma_{def} = M\alpha_{def}Gb\sqrt{N_{def}d_{def}}\ , \tag{11}$$

where M is the Taylor factor, α_{def} is the defect cluster barrier strength, G is the shear modulus, b is the magnitude of the Burger's vector ($b = 0.274$ nm for W), N_{def} is the number density of the defects, and d_{def} is the mean diameter of the defects. Combining equation (11) with the equation that correlates hardness and yield strength as proposed by Tabor [78]

$$H = k\sigma_{def}\ , \tag{12}$$

the hardening, ΔH, induced by irradiation defects can be determined through

$$\Delta H = kM\alpha_{def}Gb\sqrt{N_{def}d_{def}}\ . \tag{13}$$

In Tabor's theory the proposed value of k is 2.74. However, Hu et al. [11], following the work of Busby et al. [79], have proposed 3.20 as a more appropriate value of k. For the Taylor factor, M, W. Stoller and Zinkle [80] have recommended the value of 3.06 for non-texture BCC and FCC crystals. The value of the obstacle strength factor, α_{def}, depends on the type and size of the defects. For the dislocation loops for α_{disl} the value of 0.15 was adopted as suggested in [11]. The obstacle strength for voids depends on their size and taking into account the mean size of voids measured by TEM we can develop a scaling using the measured values of hardness. Assuming a root-sum-square law the measured ΔH is connected with the voids and loop obstacles as

$$\Delta H_{calc}^2 = \Delta H_{loop}^2 + \Delta H_{void}^2 = \left(kMGb\right)^2\left(\alpha_{loop}^2 N_{loop}d_{loop} + \alpha_{void}^2\left(d_{void}\right)N_{void}d_{void}\right) \tag{14}$$

Setting $\Delta H_{calc} = \Delta H_{\exp}$ we can calculate $\alpha_{void}\left(d_{void}\right)$ since all the other values are known. The α_{void} has been calculated in Fig. 9 using relevant TEM values and values for k, M and α_{disl} suggested by Hu et al [11] and for the shear modulus, G, that measured by IET (Table III). We observe that α_{void} and the void size are well correlated and the obtained values are in good agreement to those obtained by Hu for the corresponding sizes. Finally the hardness arising from the loop and the voids as well the total hardness are calculated (Table IV). As it can be observed in Fig. 8 and Table IV the calculated hardening, ΔH_{def}^{TEM}, is in good agreement with the experimental values within error. At 600 °C the contribution from loops to the hardening is comparable with that due to the presence of voids, whereas at 1200 °C the hardening is mainly due to the voids and the loops have a minor contribution because of the drastic decrease in their number density.

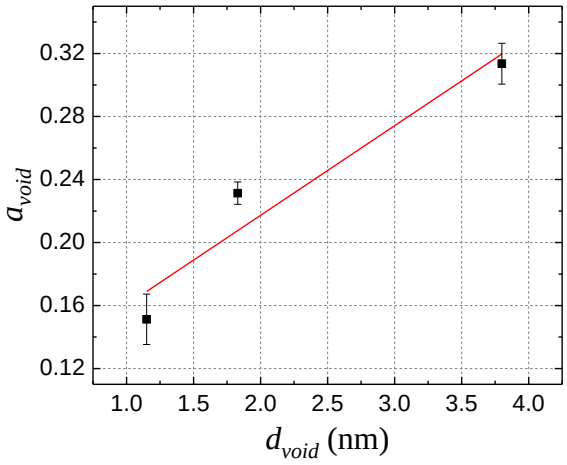

Fig. 9 . Obstacle strength versus void diameter calculated using eq. (15). The solid line is a linear least square fit.

Table IV. Experimental hardness increase, ΔH , and calculated one using the dispersion barrier hardening model and the data obtained from TEM measurements (Table I).

T_{irr} (°C)	$\Delta H_{\exp}$ (GPa)	ΔH_{voids} (GPa)	α_{void} [1]	ΔH_{loops} (GPa)	ΔH_{calc} [2] (GPa)
600	0.90 ± 0.12	0.85	0.17	0.49	0.98
800	1.29 ± 0.10	1.16	0.21	0.19	1.17
1200	1.26 ± 0.13	1.28	0.32	0.13	1.29

[1] From the least squares fitted line in Fig.9.

[2] $\Delta H_{calc} = \sqrt{\Delta H_{loop}^2 + \Delta H_{void}^2}$

4 SUMMARY AND CONCLUSIONS

Disks of about 1 mm thick of tungsten material produced by PLANSEE SE by sintering and rolling to 1 mm thickness were irradiated by fast neutrons to a damage level of 0.18 dpa and in the temperature range from 600 to 1200 °C.

Voids and dislocation loops are observed at all irradiation temperatures, with their number density decreasing and their size increasing with the increase of the irradiation temperature. The total dislocation density after irradiation at 600 °C increases by a factor of two compared with the unirradiated sample. This increase is explained by a relatively high density of the dislocation loops formed. As the temperature is raised to 800 °C the total density of dislocation decreases showing that at this temperature pre-existing dislocations are removed during the irradiation. In general, the neutron irradiation reduces the density of pre-existing bulk dislocations by a factor of three. Voids are formed after irradiation at 600 °C having a mean size of around 1.15 nm. An increase of the radiation temperature to 800 °C increases their size to 1.83 nm and their volume fraction by around three times. Further increase of the radiation

temperature to 1200 °C increases their volume fraction by a factor of two. These TEM observations are corroborated by positron annihilation spectroscopy results that show the formation of voids at all investigated irradiation temperatures with size larger than 1 nm. Furthermore, PALS also shows the formation of very small vacancy clusters in the temperature range of 800 - 900 °C.

The irradiation induced resistivity is in good agreement with the calculated values taking into account the partial contribution to the resistivity from transmutation, voids and dislocations. Therefore, three techniques TEM, positron annihilation spectroscopy and resistivity measurements give a consistent picture of the defects produced after 0.18 dpa fast neuron irradiation in the temperature range from 600 to 1200 °C.

The irradiation produced defects have no measurable influence on the elastic constants of the material. However, the hardness after irradiation at 600 °C has been increased, compared to the unirradiated sample, by 0.90 GPa. Irradiation at 800 °C results to a further increase of 0.39 GPa. Higher temperature irradiation does not change the hardness, within errors, with respect to that measured at 800 °C. The irradiation induced hardness is in good agreement with the values calculated using the dispersion hardening barrier model.

ACKNOWLEDGMENTS

This work has been carried out within the framework of the EUROfusion Consortium and has received funding from the Euratom research and training programme 2014-2018 and 2019-2020 under Grant Agreements No. 633053. The views and opinions expressed herein do not necessarily reflect those of the European Commission. Also is acknowledged the support of the programme “NCSRD – INRASTES research activities in the framework of the national RIS3" (MIS 5002559) which is implemented under the “Action for the Strategic Development on the Research and Technological Sector”, funded by the Operational Programme "Competitiveness, Entrepreneurship and Innovation" (NSRF 2014-2020) and co-financed by Greece and the European Union (European Regional Development Fund).

References

[1] M. Rieth, R. Doerner, A. Hasegawa, Y. Ueda, M. Wirtz, Behavior of tungsten under irradiation and plasma interaction, J. Nucl. Mater. 519 (2019) 334–368. https://doi.org/10.1016/j.jnucmat.2019.03.035.

[2] G. Pintsuk, Tungsten as a Plasma-Facing Material, in: Compr. Nucl. Mater., Elsevier, 2012: pp. 551–581. https://doi.org/10.1016/B978-0-08-056033-5.00118-X.

[3] S. Wurster, N. Baluc, M. Battabyal, T. Crosby, J. Du, C. García-Rosales, A. Hasegawa, A. Hoffmann, A. Kimura, H. Kurishita, R.J. Kurtz, H. Li, S. Noh, J. Reiser, J. Riesch, M. Rieth, W. Setyawan, M. Walter, J.H. You, R. Pippan, Recent progress in R&D on tungsten alloys for divertor structural and plasma facing materials, J. Nucl. Mater. 442 (2013) 181–189. https://doi.org/10.1016/j.jnucmat.2013.02.074.

[4] J. Reiser, J. Hoffmann, U. Jäntsch, M. Klimenkov, S. Bonk, C. Bonnekoh, M. Rieth, A. Hoffmann, T. Mrotzek, Ductilisation of tungsten (W): On the shift of the brittle-to-ductile transition (BDT) to lower temperatures through cold rolling, Int. J. Refract. Met. Hard Mater. 54 (2016) 351–369. https://doi.org/10.1016/j.ijrmhm.2015.09.001.

[5] C. Bonnekoh, A. Hoffmann, J. Reiser, The brittle-to-ductile transition in cold rolled tungsten: On the decrease of the brittle-to-ductile transition by 600 K to − 65 °C, Int. J. Refract. Met. Hard Mater. 71 (2018) 181–189. https://doi.org/10.1016/j.ijrmhm.2017.11.017.

[6] A. Hasegawa, T. Tanno, S. Nogami, M. Satou, Property change mechanism in tungsten under neutron irradiation in various reactors, J. Nucl. Mater. 417 (2011) 491–494. https://doi.org/10.1016/j.jnucmat.2010.12.114.

[7] A. Hasegawa, M. Fukuda, T. Tanno, S. Nogami, Neutron irradiation behavior of tungsten, Mater. Trans. 54 (2013) 466–471. https://doi.org/10.2320/matertrans.MG201208.

[8] A. Hasegawa, M. Fukuda, S. Nogami, K. Yabuuchi, Neutron irradiation effects on tungsten materials, Fusion Eng. Des. 89 (2014) 1568–1572. https://doi.org/10.1016/j.fusengdes.2014.04.035.

[9] A. Hasegawa, M. Fukuda, K. Yabuuchi, S. Nogami, Neutron irradiation effects on the microstructural development of tungsten and tungsten alloys, J. Nucl. Mater. 471 (2016) 175–183. https://doi.org/10.1016/j.jnucmat.2015.10.047.

[10] X. Hu, T. Koyanagi, M. Fukuda, Y. Katoh, L.L. Snead, B.D. Wirth, Defect evolution in single crystalline tungsten following low temperature and low dose neutron irradiation, J. Nucl. Mater. 470 (2016) 278–289. https://doi.org/10.1016/j.jnucmat.2015.12.040.

[11] X. Hu, T. Koyanagi, M. Fukuda, N.A.P.K. Kumar, L.L. Snead, B.D. Wirth, Y. Katoh, Irradiation hardening of pure tungsten exposed to neutron irradiation, J. Nucl. Mater. 480 (2016) 235–243. https://doi.org/10.1016/j.jnucmat.2016.08.024.

[12] M. Fukuda, N.A.P. Kiran Kumar, T. Koyanagi, L.M. Garrison, L.L. Snead, Y. Katoh, A. Hasegawa, Neutron energy spectrum influence on irradiation hardening and microstructural development of tungsten, J. Nucl. Mater. 479 (2016) 249–254. https://doi.org/10.1016/j.jnucmat.2016.06.051.

[13] T. Koyanagi, N.A.P.K. Kumar, T. Hwang, L.M. Garrison, X. Hu, L.L. Snead, Y. Katoh, Microstructural evolution of pure tungsten neutron irradiated with a mixed energy spectrum, J. Nucl. Mater. 490 (2017) 66–74. https://doi.org/10.1016/j.jnucmat.2017.04.010.

[14] L.M. Garrison, Y. Katoh, N.A.P.K. Kumar, Mechanical properties of single-crystal tungsten irradiated in a mixed spectrum fission reactor, J. Nucl. Mater. 518 (2019) 208–225. https://doi.org/10.1016/j.jnucmat.2019.02.050.

[15] G. Bonny, M.J. Konstantinovic, A. Bakaeva, C. Yin, N. Castin, K. Mergia, V. Chatzikos, S. Dellis, T. Khvan, A. Bakaev, A. Dubinko, D. Terentyev, Trends in vacancy distribution and hardness of high

temperature neutron irradiated single crystal tungsten, Acta Mater. 198 (2020) 1–9. https://doi.org/10.1016/j.actamat.2020.07.047.
[16] R.K. Williams, F.W. Wiffen, J. Bentley, J.O. Stiegler, Irradiation induced precipitation in tungsten based, W-Re alloys, Metall. Trans. A. 14 (1983) 655–666. https://doi.org/10.1007/BF02643781.
[17] Y. Nemoto, A. Hasegawa, M. Satou, K. Abe, Microstructural development of neutron irradiated W-Re alloys, J. Nucl. Mater. 283–287 (2000) 1144–1147. https://doi.org/10.1016/S0022-3115(00)00290-7.
[18] M. Fukuda, A. Hasegawa, T. Tanno, S. Nogami, H. Kurishita, Property change of advanced tungsten alloys due to neutron irradiation, J. Nucl. Mater. 442 (2013) S273–S276. https://doi.org/10.1016/j.jnucmat.2013.03.058.
[19] M. Fukuda, K. Yabuuchi, S. Nogami, A. Hasegawa, T. Tanaka, Microstructural development of tungsten and tungsten-rhenium alloys due to neutron irradiation in HFIR, J. Nucl. Mater. 455 (2014) 460–463. https://doi.org/10.1016/j.jnucmat.2014.08.002.
[20] J. C. He, G. Y. Tang, A. Hasegawa, K. Abe, Microstructural development and irradiation hardening of W and W–(3–26) wt%Re alloys after high-temperature neutron irradiation to 0.15 dpa, Nucl. Fusion. 46 (2006) 877–883. https://doi.org/10.1088/0029-5515/46/11/001.
[21] S. Das, Recent advances in characterising irradiation damage in tungsten for fusion power, SN Appl. Sci. 1 (2019) 1–20. https://doi.org/10.1007/s42452-019-1591-0.
[22] V.K. Sikka, J. Moteff, Superlattice of voids in neutron-irradiated tungsten, J. Appl. Phys. 43 (1972) 4942–4944. https://doi.org/10.1063/1.1661050.
[23] S. Krimpalis, K. Mergia, S. Messoloras, A. Dubinko, D. Terentyev, K. Triantou, J. Reiser, G. Pintsuk, Comparative study of the mechanical properties of different tungsten materials for fusion applications, Phys. Scr. 2017 (2017). https://doi.org/10.1088/1402-4896/aa9292.
[24] D. Pelowitz, J. Durkee, J. Elson, M. Fensin, R. Johns, G. McKinney, S. Mashnik, J. Verbeke, L. Waters, T. Wilcox, MCNPX 2.7.0 Extensions, 2011
[25] M.J. Norgett, M.T. Robinson, I.M. Torrens, A proposed method of calculating displacement dose rates, Nucl. Eng. Des. 33 (1975) 50–54. https://doi.org/10.1016/0029-5493(75)90035-7.
[26] P. Hirsch, A. Howie, R. Nicholson, D.W. Pashley, M.J. Whelan, Electron Microscopy of Thin Crystals, Krieger Publishing Company Malabar, Florida, 1977
[27] A. Dubinko, D. Terentyev, A. Bakaeva, K. Verbeken, M. Wirtz, M. Hernández-Mayoral, Evolution of plastic deformation in heavily deformed and recrystallized tungsten of ITER specification studied by TEM, Int. J. Refract. Met. Hard Mater. 66 (2017) 105–115. https://doi.org/10.1016/j.ijrmhm.2017.03.004.
[28] A. Dubinko, D. Terentyev, A. Bakaeva, T. Pardoen, M. Zibrov, T.W. Morgan, Effect of high flux plasma exposure on the micro-structural and -mechanical properties of ITER specification tungsten, Nucl. Instruments Methods Phys. Res. Sect. B Beam Interact. with Mater. Atoms. 393 (2017) 155–159. https://doi.org/10.1016/j.nimb.2016.10.041.
[29] A. Dubinko, D. Terentyev, A. Bakaeva, M. Hernández-Mayoral, G. De Temmerman, L. Buzi, J.M. Noterdaeme, B. Unterberg, Sub-surface microstructure of single and polycrystalline tungsten after high flux plasma exposure studied by TEM, Appl. Surf. Sci. 393 (2017) 330–339. https://doi.org/10.1016/j.apsusc.2016.09.071.
[30] A. Dubinko, A. Bakaeva, M. Hernández-Mayoral, D. Terentyev, G. De Temmerman, J.M. Noterdaeme, Microstructural modifications in tungsten induced by high flux plasma exposure: TEM examination, Phys. Scr. 2016 (2016). https://doi.org/10.1088/0031-8949/T167/1/014030.
[31] Positrons in Solids, in: P. Hautojarvi (Ed.), Topics in Current Physics, Vol. 12, Springer-Verlag Berlin Heidelberg, New York, 1979. https://doi.org/10.1007/978-3-642-81316-0.

[32] M. Eldrup, B.N. Singh, Studies of defects and defect agglomerates by positron annihilation spectroscopy, J. Nucl. Mater. 251 (1997) 132–138. https://doi.org/10.1016/S0022-3115(97)00221-3.
[33] D. Giebel, J. Kansy, LT10 Program for Solving Basic Problems Connected with Defect Detection, Phys. Procedia. 35 (2012) 122–127. https://doi.org/10.1016/j.phpro.2012.06.022.
[34] D. Giebel, J. Kansy, A new version of LT program for Positron Lifetime Spectra Analysis, Mater. Sci. Forum. 666 (2011) 138–141. https://doi.org/10.4028/www.scientific.net/MSF.666.138.
[35] G. Dlubek, A. Sen Gupta, J. Pionteck, R. Häßler, R. Krause-Rehberg, H. Kaspar, K.H. Lochhaas, Glass transition and free volume in the mobile (MAF) and rigid (RAF) amorphous fractions of semicrystalline PTFE: a positron lifetime and PVT study, Polymer (Guildf). 46 (2005) 6075–6089. https://doi.org/10.1016/j.polymer.2005.04.090.
[36] O. V. Ogorodnikova, M. Majerle, V. V. Gann, J. Čížek, P. Hruška, S. Simakov, M. Štefánik, V. Zach, Verification of the theory of primary radiation damage by comparison with experimental data, J. Nucl. Mater. 525 (2019) 22–31. https://doi.org/10.1016/j.jnucmat.2019.07.019.
[37] G.S. Kanda, L. Ravelli, B. Löwe, W. Egger, D.J. Keeble, Positron annihilation lifetime spectroscopy study of Kapton thin foils, J. Phys. D. Appl. Phys. 49 (2016) 025305. https://doi.org/10.1088/0022-3727/49/2/025305.
[38] M.J. Konstantinović, G. Bonny, Thermal stability and the structure of vacancy-solute clusters in iron alloys, Acta Mater. 85 (2015) 107–111. https://doi.org/10.1016/j.actamat.2014.11.026.
[39] M.J. Konstantinović, I. Uytdenhouwen, G. Bonny, N. Castin, L. Malerba, P. Efsing, Radiation induced solute clustering in high-Ni reactor pressure vessel steel, Acta Mater. 179 (2019) 183–189. https://doi.org/10.1016/j.actamat.2019.08.028.
[40] R.A. Weller, An algorithm for computing linear four-point probe thickness correction factors, Rev. Sci. Instrum. 72 (2001) 3580–3586. https://doi.org/10.1063/1.1394186.
[41] I. Miccoli, F. Edler, H. Pfnür, C. Tegenkamp, The 100th anniversary of the four-point probe technique: The role of probe geometries in isotropic and anisotropic systems, J. Phys. Condens. Matter. 27 (2015). https://doi.org/10.1088/0953-8984/27/22/223201.
[42] G. Martinček, The determination of poisson's ratio and the dynamic modulus of elasticity from the frequencies of natural vibration in thick circular plates, J. Sound Vib. 2 (1965) 116–127. https://doi.org/10.1016/0022-460X(65)90089-1.
[43] ASTM Standard E1876–01, Standard Test Method for Dynamic Young's Modulus, Shear Modulus, and Poisson's Ratio by Impulse Excitation of Vibration, ASTM Int. (2005) 16. doi:10.1520/E1876-09.
[44] J.M. Campillo Robles, F. Plazaola, Collection of data on positron lifetimes and vacancy formation energies of the elements of the periodic table, Defect Diffus. Forum. 213–215 (2003) 141–236. https://doi.org/10.4028/www.scientific.net/ddf.213-215.141.
[45] M.J. Puska, Ab-initio calculation of positron annihilation rates in solids, J. Phys. Condens. Matter. 3 (1991) 3455–3469. https://doi.org/10.1088/0953-8984/3/20/007.
[46] T.E.M. Staab, R. Krause-Rehberg, B. Vetter, B. Kieback, The influence of microstructure on the sintering process in crystalline metal powders investigated by positron lifetime spectroscopy: I. Electrolytic and spherical copper powders, J. Phys. Condens. Matter. 11 (1999) 1757–1786. https://doi.org/10.1088/0953-8984/11/7/009.
[47] S. Zhu, Y. Xu, Z. Wang, Y. Zheng, D. Zhou, E. Du, D. Yuan, M. Fukuda, M. Mihara, K. Matsuta, T. Minamisono, Positron annihilation lifetime spectroscopy on heavy ion irradiated stainless steels and tungsten, J. Nucl. Mater. 343 (2005) 330–332. https://doi.org/10.1016/j.jnucmat.2004.11.024.
[48] T. Troev, E. Popov, N. Nankov, T. Yoshiie, Model calculation of positron states in tungsten containing hydrogen and helium, J. Phys. Conf. Ser. 207 (2010). https://doi.org/10.1088/1742-6596/207/1/012033.

[49] P. Staikov, N. Djourelov, Simulations of 〈1 0 0〉 edge and 1/2〈1 1 1〉 screw dislocations in α-iron and tungsten and positron lifetime calculations, Phys. B Condens. Matter. 413 (2013) 59–63. https://doi.org/10.1016/j.physb.2012.12.026.
[50] J. Heikinheimo, K. Mizohata, J. Räisänen, T. Ahlgren, P. Jalkanen, A. Lahtinen, N. Catarino, E. Alves, F. Tuomisto, Direct observation of mono-vacancy and self-interstitial recovery in tungsten, APL Mater. 7 (2019). https://doi.org/10.1063/1.5082150.
[51] P.E. Lhuillier, M.F. Barthe, P. Desgardin, W. Egger, P. Sperr, Positron annihilation studies on the nature and thermal behaviour of irradiation induced defects in tungsten, Phys. Status Solidi. 6 (2009) 2329–2332. https://doi.org/10.1002/pssc.200982114.
[52] A. Yabuuchi, M. Tanaka, A. Kinomura, Short positron lifetime at vacancies observed in electron-irradiated tungsten: Experiments and first-principles calculations, J. Nucl. Mater. 542 (2020) 152473. https://doi.org/10.1016/j.jnucmat.2020.152473.
[53] X. Hu, T. Koyanagi, M. Fukuda, Y. Katoh, L.L. Snead, B.D. Wirth, Defect evolution in single crystalline tungsten following low temperature and low dose neutron irradiation, J. Nucl. Mater. 470 (2016) 278–289. https://doi.org/10.1016/j.jnucmat.2015.12.040.
[54] C.L. Dube, P.K. Kulriya, D. Dutta, P.K. Pujari, Y. Patil, M. Mehta, P. Patel, S.S. Khirwadkar, Positron annihilation lifetime measurement and X-ray analysis on 120 MeV Au+7 irradiated polycrystalline tungsten, J. Nucl. Mater. 467 (2015) 406–412. https://doi.org/10.1016/j.jnucmat.2015.05.029.
[55] P.M.G. Nambissan, P. Sen, Positron annihilation study of the annealing behaviour of alpha induced defects in tungsten, Radiat. Eff. Defects Solids. 124 (1992) 215–221. https://doi.org/10.1080/10420159208220193.
[56] P.D. Desai, T.K. Chu, H.M. James, C.Y. Ho, Electrical Resistivity of Selected Elements, J. Phys. Chem. Ref. Data. 13 (1984) 1069–1096. https://doi.org/10.1063/1.555723.
[57] G.K. White, M.L. Minges, Thermophysical properties of some key solids: An update, Int. J. Thermophys. 18 (1997) 1269–1327. https://doi.org/10.1007/BF02575261.
[58] P.L. Rossiter, The electrical resistivity of metals and alloys, Cambridge University Press, Cambridge, 1987, pp. 195-198. https://doi.org/10.1017/CBO9780511600289.
[59] P.L. Rossiter, The electrical resistivity of metals and alloys, Cambridge University Press, Cambridge, 1987, pp. 127-136, pp. 195-198. https://doi.org/10.1017/CBO9780511600289.
[60] J.W. Martin, The electrical resistivity due to structural defects, Philos. Mag. 24 (1971) 555–566. https://doi.org/10.1080/14786437108217029.
[61] J.W. Martin, The electrical resistivity of some lattice defects in FCC metals observed in radiation damage experiments, J. Phys. F Met. Phys. 2 (1972) 842–853. https://doi.org/10.1088/0305-4608/2/5/008.
[62] J.W. Martin, R. Paetsch, Electrical resistivity of voids, J. Phys. F Met. Phys. 3 (1973) 907–917. https://doi.org/10.1088/0305-4608/3/5/005.
[63] K.D. Rasch, R.W. Siegel, H. Schultz, Quenching and recovery investigations of vacancies in tungsten, Philos. Mag. A Phys. Condens. Matter, Struct. Defects Mech. Prop. 41 (1980) 91–117. https://doi.org/10.1080/01418618008241833.
[64] L. Uray, P. Tekula-Buxbaum, Resistivity contribution of solutes in tungsten, J. Less-Common Met. 123 (1986) 95–100. https://doi.org/10.1016/0022-5088(86)90119-0.
[65] ASM Handbook Volume 2: Properties and Selection – Nonferrous Alloys and Special-Purpose Materials", ASM International, (1992), p. 1766.
[66] B.R. Watts, The contribution of the long-range strain field of dislocations in metals to their electrical resistivity, J. Phys. F Met. Phys. 18 (1988) 1183–1195. https://doi.org/10.1088/0305-4608/18/6/021.

[67] R.A. Brown, Resonance Scattering and the Electrical and Thermal Resistivities Associated with Extended Defects in Crystals, Phys. Rev. 156 (1967) 692–700. https://doi.org/10.1103/PhysRev.156.692.
[68] Z.S. Basinski, J.S. Dugdale, A. Howie, The electrical resistivity of dislocations, Philos. Mag. 8 (1963) 1989–1997. https://doi.org/10.1080/14786436308209092.
[69] H.B. Shukovsky, R.M. Rose, J. Wulff, The low temperature electrical resistivity of lattice defects in deformed tungsten single crystals, Acta Metall. 14 (1966) 821–830. https://doi.org/10.1016/0001-6160(66)90002-2.
[70] R.A. Brown, Electrical resistivity of dislocations in metals, J. Phys. F Met. Phys. 7 (1977) 1283–1295. https://doi.org/10.1088/0305-4608/7/7/026.
[71] A.S. Karolik, A.A. Luhvich, Calculation of electrical resistivity produced by dislocations and grain boundaries in metals, J. Phys. Condens. Matter. 6 (1994) 873–886. https://doi.org/10.1088/0953-8984/6/4/007.
[72] M. Kaveh, N. Wiser, Correlation between electron-dislocation scattering and electron-impurity scattering in metals, J. Phys. F Met. Phys. 11 (1981) 1749–1763. https://doi.org/10.1088/0305-4608/11/9/004.
[73] M. Kaveh, N. Wiser, Electrical resistivity of dislocations in metals, J. Phys. F Met. Phys. 13 (1983) 953–961. https://doi.org/10.1088/0305-4608/13/5/009.
[74] F.H. Featherston, J.R. Neighbours, Elastic constants of tantalum, tungsten, and molybdenum, Phys. Rev. 130 (1963) 1324–1333. https://doi.org/10.1103/PhysRev.130.1324.
[75] D.I. Bolef, J. De Klerk, Elastic Constants of Single-Crystal Mo and W between 77° and 500°K, J. Appl. Phys. 33 (1962) 2311–2314. https://doi.org/10.1063/1.1728952.
[76] R. Lowrie, A.M. Gonas, Single-Crystal Elastic Properties of Tungsten from 24° to 1800°C, J. Appl. Phys. 38 (1967) 4505–4509. https://doi.org/10.1063/1.1709158.
[77] S.J. Zinkle, Y. Matsukawa, Observation and analysis of defect cluster production and interactions with dislocations, J. Nucl. Mater. 329–333 (2004) 88–96. https://doi.org/10.1016/j.jnucmat.2004.04.298.
[78] D. Tabor, The physical meaning of indentation and scratch hardness, Br. J. Appl. Phys. 7 (1956) 159–166. https://doi.org/10.1088/0508-3443/7/5/301.
[79] J.T. Busby, M.C. Hash, G.S. Was, The relationship between hardness and yield stress in irradiated austenitic and ferritic steels, J. Nucl. Mater. 336 (2005) 267–278. https://doi.org/10.1016/j.jnucmat.2004.09.024.
[80] R.E. Stoller, S.J. Zinkle, On the relationship between uniaxial yield strength and resolved shear stress in polycrystalline materials, J. Nucl. Mater. 283–287 (2000) 349–352. https://doi.org/10.1016/S0022-3115(00)00378-0.